MICROCHEMICAL ANALYSIS OF THE FUEL-SHEATH INTERFACE IN A POWER-RAMPED CANDU FUEL BY IMAGING-XPS

W.H. HOCKING, K.G. IRVING and THAN DO

Corrosion and Surface Science Branch
AECL, Chalk River Laboratories
Chalk River, Ontario, Canada, K0J 1P0

ABSTRACT

A detailed study of the microchemistry at the fuel-sheath interface in an intact outer element from a power-ramped CANDU fuel bundle has been conducted by imaging X-ray photoelectron spectroscopy (XPS). The power ramp caused several other elements in this bundle to fail by stress-corrosion cracking. An abundance of fission products, especially cesium, was found on all sheath and end-cap surfaces, and a number of segregated impurities, most notably sodium, were also identified. These findings suggest that iodine may not be the sole causative agent for stress-corrosion cracking of Zircaloy fuel sheath. The CANLUB layer was partly retained on the sheath and partly on the fuel pellets—different regions could be identified for microchemical XPS analysis by *in situ* scanning electron microscopy (SEM).

1. INTRODUCTION

A number of fission products that have limited solubility in the uraninite lattice tend to segregate to the grain boundaries in CANDU fuels and eventually accumulate at the fuel-sheath interface [1-7]. The rates of the migration processes involved are strongly dependent upon the fuel burnup and operating power as well as the fuel design. Fission-product segregation can become a limiting factor on fuel performance in-reactor and significantly enhances the potential for release of radioactivity during subsequent storage or after disposal as well [3-6]. The thin-walled Zircaloy-4 sheath used on CANDU fuels, which collapses onto the fuel pellets under the primary coolant pressure, was initially found to be quite susceptible to stress-corrosion cracking (SCC) [6]. Although iodine was identified as the probable causative agent of the SCC, based upon its chemical reactivity with zirconium and other indirect evidence, several studies have indicated that cesium and cadmium could also be effective SCC agents [6,8,9].

Introduction of the thin CANLUB graphite coating on the sheath interior surface virtually eliminated SCC problems for natural uranium fuels in the current CANDU power reactors under standard operating conditions [6]. Although the graphite was initially thought to function as a pellet lubricant that could reduce sheath stresses, it has subsequently been shown to play a more important role as a fission-product chemical barrier [6]. There is also some evidence that the CANLUB layer mediates evolution of the oxygen potential in CANDU fuels, which in turn may influence the chemical speciation and migration of several key fission products [1,10,11]. The

apparent disappearance of the CANLUB layer with extended burnup has been previously observed through conventional post-irradiation examinations [10]. An improved understanding of the mechanisms involved in the function and degradation of the CANLUB layer has now begun to emerge from recent studies, which could lead to the development of an improved system for more demanding applications in advanced reactors [12].

As part of an on-going fuel-performance evaluation, a CANDU bundle was subjected to a sustained power ramp following irradiation in the NRU research reactor at comparatively low power in a steep axial neutron flux gradient to about the median burnup for a natural uranium fuel. Although neither the peak power nor the maximum power increment exceeded the thresholds for which SCC would be predicted, several elements failed. A detailed study of the microchemistry at the fuel-sheath interface in an intact outer element from this bundle has been conducted by imaging X-ray photoelectron spectroscopy (XPS). Sheath and end-cap samples taken from both the lower and higher power ends of the element were characterized; in addition, fragments of fuel were selected to allow examination of the pellet periphery. The CANLUB layer was partly retained on the fuel sheath and partly adhered to the fuel pellets—different regions on each sample could be identified for XPS microchemical analysis by *in situ* scanning electron microscopy (SEM).

2. EXPERIMENTAL PROCEDURES

Because the initial irradiation of the power-ramped bundle occurred in a steep axial neutron flux gradient, its power history varied widely as a function of distance from the reference end (top). This is approximately captured by the key ratings for the top (T), middle (M) and bottom (B) of an outer element as follows: maximum linear power before ramp of 43 (T), 36 (M) and 28 (B) kW/m; linear power immediately prior to ramp of 32 (T), 28 (M) and 22 (B) kW/m; power after ramp of 44 (T), 45 (M) and 46 (B) kW/m, sustained for ~10 h; final burnup of 205 (T), 175 (M) and 140 (B) MWh/kg U. The largest power ramp (24 kW/m) thus occurred at the bottom end of the element, which had the lowest burnup and prior operating power. Mass spectrometric analysis of the gas released upon puncture of the sheath just before sample preparation (42.4% He, 7.82% Kr and 49.5% Xe, representing ~3% fission-gas release) confirmed that the selected element had remained intact.

Precautions were taken to minimize the risk of surface alteration or contamination during all sample-handling operations. Previously developed procedures that involve only dry cutting techniques were employed to obtain small samples (~5 mm by ~7 mm) from the sheath and both end caps [7,12]. The former were taken in pairs, separated by 180° and facing toward or away from the bundle centre, at distances of ~140 mm and ~103 mm from the bottom and top ends of the element respectively. Axial locations corresponding to the approximate middle of the long axis of the sheath samples were intentionally chosen to coincide with likely pellet-pellet interfaces that had been identified by visual inspection. In addition, fragments of fuel (~4 mm in size) were selected from the periphery of a pellet located near the middle of the element. All samples were affixed, with conductive, silver-based epoxy, to stainless-steel foils that could be secured within a recessed area on a custom-designed sample-transfer mount. This arrangement minimizes the potential for spreading loose contamination from the sample to the instrument.

The active Imaging-XPS facility is based upon an ESCALAB 220i-XL instrument manufactured by VG Scientific, which has been specifically configured for safe handling of highly radioactive materials [12]. Photoelectron emission was excited from the sample surfaces by a focussed beam of X-rays, with high spectral purity, provided by a monochromator that uses a pair of bent silicon crystals to filter Al Kα radiation (hν = 1486.6 eV). Although the diameter of the illuminated area can be adjusted, from ~1 mm to ~100 μm, an X-ray spot size of ~500 μm was employed for all experiments conducted in the present study. The computer-controlled electron spectrometer, which consists of magnetic and electrostatic lenses and a concentric hemispherical analyzer, was then used to further restrict the analysis area as required. An array of six channel electron multipliers provides high sensitivity and dynamic range for photoelectron spectroscopy. The spectrometer dispersion and work function were calibrated using gold, copper and silver standards with the binding-energy scale referenced to the Fermi level [13]. Static charging of the samples under the X-rays was always minor, and (if needed) it could also be neutralized by continuously flooding the surface with low-energy electrons [14].

A magnified image of the sample in the analysis chamber is produced by a video camera attached to an optical microscope and displayed on a monitor at the operator's console. This allows the sample to be observed continuously as it is being moved using the microprocessor controlled five-axis stage. An auxiliary Schottky field-emission electron gun, which is also mounted directly on the instrument analysis chamber, provides *in situ* capabilities for scanning Auger microscopy (SAM) and scanning electron microscopy (SEM). The electron spectrometer is used for Auger electron spectroscopy and a shielded secondary electron detector has been installed to allow SEM on radioactive materials. Precise alignment of the electron and X-ray beams at the focal point of the electron spectrometer was routinely checked using imaging standards.

Information on the near-surface composition as a function of depth was compiled by sequential XPS analysis and argon-ion sputter etching. The latter was performed in a custom-designed pocket chamber that is separated from the analysis chamber by a preparation chamber. This double isolation strategy was employed to avoid radioactive contamination of the sensitive detectors used for electron spectroscopy and microscopy. A focussed, normal-incident, 4 keV Ar^+ beam, with a current of 1.3 μA, was rastered over the full area (~5 mm by ~7 mm) of the sample surface. Under these conditions, the sputter-etching rate has been determined to be 0.5 nm/min using an oxide thin-film standard [15]. The *in situ* SEM capability was essential for precisely locating the same features for XPS analysis after each ion-sputter interval.

3. RESULTS

Secondary electron images collected at increasing magnification from a typical area on the inside surface of the fuel sheath toward the bottom end of the element are displayed in Figure 1. The bright band at the bottom of the lower magnification image on the left arises from the edge of the cover plate (with a central rectangular hole) that captures the sheath specimen within the recessed well on the sample-transfer mount. Patches of retained CANLUB (darker grey) are easily distinguished here from regions in which the sheath has been exposed (lighter grey). Microchemical XPS analysis of the different types of regions (see below) would not have been

feasible without the *in situ* SEM capability to identify them. Similar images were obtained from all of the other fuel-sheath samples.

The morphology on the periphery of a fuel pellet located near the middle of the element is illustrated by secondary electron images that have been reproduced in Figure 2; these images were collected from a small fragment of fuel. Conductive silver epoxy, which was used to affix the fragment to a stainless-steel foil, covers a good portion of the fracture face in the foreground of the low magnification image on the left and extends up onto the pellet periphery at the front corners. Several patches of CANLUB that were retained on the pellet periphery are easily distinguished (darker grey) from the exposed fuel surface (lighter grey). One such patch is shown in further detail by the higher magnification image on the right in Figure 2.

Representative XPS survey spectra that were recorded from regions with and without a visible CANLUB layer on a fuel-sheath sample taken from toward the bottom end of the element are compared in Figure 3—they are surprisingly similar. In both cases, the Cs 3d spin-orbit doublet is the dominant feature, followed by peaks arising from the C 1s and O 1s core levels. Quantitative analysis of the XPS data revealed that carbon (>50 at.%) and oxygen (>25 at.%) were actually more abundant than cesium (<10 at.%) at the surface (the C 1s level has quite a small photoelectron cross-section, whereas the cross-sections for the Cs 3d and U 4f doublets are especially large). Comparable amounts of uranium, copper, sodium, chlorine, rubidium, iodine, xenon, and barium were also detected at lower levels (not all minor peaks have been labelled). The most significant difference here is the greater intensity of the Zr 3d and Zr 3p emissions from the region without a visible CANLUB layer.

Representative XPS survey spectra that were recorded from regions with and without a visible CANLUB layer on a fuel-sheath sample taken from toward the top end of the element are compared in Figure 4. These spectra are again remarkably similar to each other as well as to those displayed in Figure 3. In particular, carbon (>50 at.%) and oxygen (>25 at.%) followed by cesium (<10 at.%) are consistently the most abundant elements at the surface, regardless of the location. Subtle differences in the relative proportions of the minor species can be identified, e.g., the emission features arising from iodine, tellurium and barium are all stronger in Figure 4 than Figure 3, whereas those due to copper and xenon are weaker.

A sequence of XPS spectra that were recorded from a typical region without a visible CANLUB layer after increasing intervals of argon-ion sputtering has been reproduced in Figure 5; it reveals a complex thin film. The intensity of the C 1s peak increases over the initial few minutes of sputtering to a relatively high level, which is then maintained through several cycles before decreasing markedly following the longest sputter. A similar overall pattern is observed for the U 4f and I 3d spin-orbit doublets, although the latter decreases somewhat more quickly after the longer intervals. The zirconium emission features progressively increase in strength as a function of sputtering throughout the depth profile, whereas most of the fission products, including Rb, Te and Cs, exhibit the converse behaviour.

Chemical-shift effects for the Zr 3d and Zr 3p doublets indicate that zirconium is primarily in the elemental state after 150 min of argon-ion sputtering—consistent with sampling of the underlying alloy. Following removal of adventitious contamination by the initial sputter, the

shape and position of the C 1s peak are characteristic of graphite, although the shoulder that develops on the low-binding energy side toward the end of the depth profile indicates some carbide formation [16]. Significant oxidation of uranium beyond the tetravalent state has been observed only at the surface, whereas broadening on the low-binding energy side of each component of the U 4f doublet after 150 min of sputtering suggests partial reduction of uranium to the elemental state [16]. Tellurium is in a tetravalent state at the surface and otherwise in a reduced form (elemental or telluride) [16]. Conversely, cesium and iodine remain in the same valence states, +1 and –1 respectively, throughout the depth profile [16].

A sequence of XPS spectra that were recorded from a typical region with a visible CANLUB layer after increasing intervals of argon-ion sputtering has been reproduced in Figure 6. The comparative weakness of the Zr 3d and Zr 3p spin-orbit doublets here represents the most significant difference from Figure 5. Indeed, observation of zirconium even at modest levels is surprising for a location where the sheath is covered by an apparently intact CANLUB layer. The C 1s and U 4f emission features again increase rapidly in strength over the initial few minutes of sputtering, but then remain at a higher level to the end of the depth profile. Decreases in the intensities of the I 3d and Cs 3d doublets after the longer sputter periods are also less pronounced than in Figure 5, whereas the Te 3d emission is relatively weak from the outset.

The increase in zirconium in lower oxidation states as a function of depth is much less apparent in Figure 6 than in Figure 5 and may largely reflect preferential sputtering effects. There is also no indication of carbide formation or the presence of elemental uranium by the end of the depth profile in Figure 6. Otherwise, the chemistry at these two types of locations is similar: with carbon in the form of graphite, uranium mainly in the tetravalent state except at the surface, and cesium and iodine in +1 and –1 valence states respectively throughout [16].

Representative XPS survey spectra that were recorded from typical regions (CANLUB patches and exposed fuel) identified on the periphery of the fuel fragment shown in Figure 2 are compared in Figure 7. The Cs 3d spin-orbit doublet is again the dominant feature in both spectra, but the U 4f doublet is now the next strongest emission. Aside from the stronger U 4f doublet, the lower spectrum in Figure 7 is qualitatively similar to those recorded from CANLUB layers retained on the sheath, including the detection of zirconium, iodine, rubidium, sodium and chlorine (not labelled) at minor levels. The exposed fuel surface shows surprisingly weak C 1s emission.

A comparison of typical XPS survey spectra recorded from the inside surface of each end cap is presented in Figure 8; these show some similarities to, as well as notable differences from, the fuel-sheath spectra. In both cases, the Cs 3d doublet is again quite strong, albeit no longer dominant, whereas the C 1s emission is comparatively weak and the I 3d doublet is at the detection limit. The spectrum obtained from the bottom end of the element (which operated at low power prior to the ramp) exhibits unusually strong U 4f and Na 1s peaks. Conversely, these emission features are relatively weak in the spectrum recorded from the top end of the element, whereas the Zr 3d and Ba 3d doublets are particularly strong. The Te 3d doublet has above average intensity in both spectra and shows clear evidence of reduced as well as oxidized tellurium on the top end cap.

4. DISCUSSION

A previous XPS study of a CANDU fuel that had been operated under more normal conditions revealed only modest levels of fission-product segregation, except at the end caps [12]. Based upon their local concentration at former pellet-pellet interfaces, the primary migration route for the fission products was inferred to have been axially to the pellet ends and then radially to the sheath. The comparatively uniform distribution and abundance of fission products, especially cesium, found here can therefore be attributed largely to the effects of the power ramp. Infiltration of fission products along as well as into the CANLUB graphite layer was clearly efficient and helps to explain its effectiveness as a chemical barrier. Retention of a thin film of graphite on the sheath at locations where the bulk of the CANLUB layer had separated with the fuel would also have been beneficial.

The high abundance of cesium relative to iodine and rubidium in all of the microchemical XPS analyses of the power-ramped fuel is entirely consistent with the fission yields for these elements ($Y_I \approx Y_{Rb} \approx 0.1 \cdot Y_{Cs}$) [7]. Significant enrichment of iodine or rubidium with respect to cesium at the fuel sheath would not have been expected, because previous studies have typically indicated similar migration behaviour [7]. Conversely, a deficiency at the fuel sheath of barium, which is partly created by decay of ^{134}Cs and ^{137}Cs, is entirely consistent with its generally lower segregation tendency, although the findings for the top end cap (Figure 8) indicate a strong temperature dependence. Sodium is a minor impurity in the fuel, the CANLUB and the Zircaloy-4 [17] that should segregate in a similar fashion to the alkali metal fission products; however, the comparatively high levels found here suggest additional contamination, possibly introduced during element fabrication.

Although previous attention has focussed mainly on iodine as the causative agent for SCC of Zircaloy fuel sheath [6], relative abundance considerations alone suggest that the alkali metals collectively are more likely to have been the primary cause of the element failures here. Cesium has been shown through single-effect experiments to be at least as effective an SCC agent as iodine for zirconium alloys [8], and sodium as well as rubidium might be expected to behave in a similar fashion [18]. The potential role of impurities, such as sodium, in fuel performance, which may offer an explanation for failures below predicted thresholds, would thus appear to warrant further investigation.

The presence of uranium oxide at modest concentrations throughout the CANLUB layer has been demonstrated by extensive XPS composition depth profiling—in previous studies [12] as well as the present work. Thermal evaporation of uranium from the pellet surfaces would be negligible at the fuel-sheath operating temperatures; instead, radiation-induced migration of urania into the thin CANLUB layer is the more plausible interpretation. The daughter nuclides created by fission, which have initial energies of 67-95 MeV, can travel distances of 6-9 μm within the fuel matrix [19-21]. Collision cascades that reach the pellet periphery will cause recoil implantation of atoms and molecular fragments into the evolving interfacial layer. Transient vaporization of fuel material will also occur at any location where a fission fragment emerges from a pellet surface at high velocity, due to thermal-spike and pressure-gradient effects. Progressive radiation damage of the CANLUB layer must occur as well from the onset of the irradiation. Further evidence of these energetic processes is provided by the observation

of a modest graphite contribution to the growing deposits on the end caps and the identification of some carbide within exposed sheath surfaces. Introduction of increasing amounts of segregated fission products plus urania and zirconia into the evolving interfacial layer will augment the radiation damage. Physical loss of material during preparation of metallographic cross-sections, because of degraded mechanical integrity, therefore likely contributes to the apparent disappearance of CANLUB that has been reported at high burnup.

5. CONCLUSIONS

New insight into fission-product segregation properties and migration routes is emerging from microchemical XPS studies of the fuel-sheath interface in CANDU fuels with diverse irradiation histories. The mechanisms involved in the function and degradation of the CANLUB layer have also been further elucidated. Causative agents for stress-corrosion cracking of the Zircaloy-4 fuel sheath include cesium and possibly sodium as well as iodine. An advanced CANLUB system, which could provide robust protection of the sheath under severe operating conditions and to extended burnup, would comprise multiple barriers and fully accommodate radiation damage.

6. ACKNOWLEDGEMENTS

The authors would like to acknowledge the skilled work of the Hot Cells staff at CRL, especially R.E. Moeller and D.V. O'Brien, in preparing the fuel samples.

7. REFERENCES

1. H. Kleykamp, "The Chemical State of the Fission Products in Oxide Nuclear Fuels", Journal of Nuclear Materials, 131, 221-246 (1985).
2. Hj. Matzke, "Atomic Transport Properties in UO_2 and Mixed Oxides $(U,Pu)O_2$", Journal of the Chemical Society, Faraday Transactions 2, 83, 1121-1142 (1987).
3. J.R. Matthews, "Technological Problems and the Future of Research on the Basic Properties of Actinide Oxides", Journal of the Chemical Society, Faraday Transactions 2, 83, 1273-1285 (1987).
4. L.H. Johnson and D.W. Shoesmith, "Spent Fuel", in "Radioactive Waste Forms for the Future", Edited by W. Lutze and R.C. Ewing, Elsevier Science, Amsterdam, Chapter 11, 635-698 (1988).
5. J.H. Gittus, J.R. Matthews and P.E. Potter, "Safety Aspects of Fuel Behaviour During Faults and Accidents in Pressurised Water Reactors and in Liquid Sodium Cooled Fast Breeder Reactors", Journal of Nuclear Materials, 166, 132-159 (1989).
6. B. Cox, "Pellet-Clad Interaction (PCI) Failures of Zirconium Alloy Fuel Cladding—A Review", Journal of Nuclear Materials, 172, 249-292 (1990).
7. W.H. Hocking, A.M. Duclos and L.H. Johnson, "Study of Fission-Product Segregation in Used CANDU Fuel by X-Ray Photoelectron Spectroscopy (XPS) II", Journal of Nuclear Materials, 209, 1-26 (1994).

8. B. Cox, B.A. Surette and J.C. Wood, "Pellet-Clad Interaction Failures: Stress Corrosion Cracking by Iodine or Metal Vapour Embrittlement by Cesium/Cadmium Vapours?", Proceedings of the 2nd International Conference on Environmental Degradation of Engineering Materials, Volume 2, 293-302 (1981).
9. R. Haddad and B. Cox, "On the Initiation of Cracks in Zircaloy Tubes by I_2 and Cs/Cd Vapours", Journal of Nuclear Materials, 138, 81-88 (1986).
10. M.R. Floyd, J. Novak and P.T. Truant, "Fission-Gas Release in Fuel Performing to Extended Burnups in Ontario Hydro Nuclear Generating Stations", Atomic Energy of Canada Limited Report, AECL-10636 (1992).
11. W.H. Hocking and F.J. Szostak, "Measurement of the Composition of the Noble-Metal Particles in High-Burnup CANDU Fuel by Wavelength Dispersive X-Ray Microanalysis", Proceedings of the 6th International Conference on CANDU Fuel, Niagara Falls, Volume 1, Edited by R. Sejnoha, Canadian Nuclear Society, Toronto, 127-142 (1999), also Atomic Energy of Canada Limited Report, AECL-12055 (1999).
12. W.H. Hocking and K.G. Irving, "Microchemical Studies of Irradiated Fuel by Imaging-XPS", Proceedings of the 7th International Conference on CANDU Fuel, Kingston, Volume 1, Edited by B.J. Lewis, Canadian Nuclear Society, Toronto, 163-175 (2001), also Atomic Energy of Canada Limited Report, AECL-12135 (2001).
13. M.P. Seah, I.S. Gilmore and G. Beamson, "XPS: Binding Energy Calibration of Electron Spectrometers 5—Re-evaluation of the Reference Energies", Surface and Interface Analysis, 26, 642-649 (1998).
14. M.P. Seah, "Charge Referencing Techniques for Insulators", Appendix 2 in "Practical Surface Analysis", Second Edition, Volume 1, "Auger and X-Ray Photoelectron Spectroscopy", Edited by D. Briggs and M.P. Seah, Wiley, Chichester, 541-554 (1990).
15. W.H. Hocking, R.A. Verrall, P.G. Lucuta and Hj. Matzke, "Depth-Profiling Studies of Ion-Implanted Cesium and Rubidium in SIMFUEL and Uranium Dioxide", Radiation Effects and Defects in Solids, 125, 299-321 (1993).
16. J.F. Moulder, W.F. Stickle, P.E. Sobol and K.D. Bomben, "Handbook of X-Ray Photoelectron Spectroscopy", Edited by J. Chastain and R.C. King, Jr., Physical Electronics, Eden Prairie (1995).
17. J.C. Tait and J.R. Theaker, "Light Element Radionuclides in Used Fuel and Their Potential Contribution to Postclosure Safety Assessment", Atomic Energy of Canada Limited Report, AECL-11431 (1996).
18. B. Cox and Y.M. Wong, "Liquid Metal Embrittlement of Zr-2.5%Nb Alloy", Journal of Nuclear Materials, 245 (1997) 34-43.
19. Hj. Matzke, "Radiation Damage in Crystalline Insulators, Oxides and Ceramic Nuclear Fuels", Radiation Effects, 64, 3-33 (1982).
20. Hj. Matzke, "Irradiation Damage and Fission Product Behaviour in Ceramic Nuclear Fuels", in "High Temperature Ceramics", Edited by P. Vincenzini, Elsevier Science, Amsterdam, 2799-2808 (1987).
21. T. Wiss, Hj. Matzke, C. Trautmann, M. Toulemonde and S. Klaumunzer, "Radiation Damage in UO_2 by Swift Heavy Ions", Nuclear Instruments and Methods in Physics Research B, 122, 583-588 (1997).

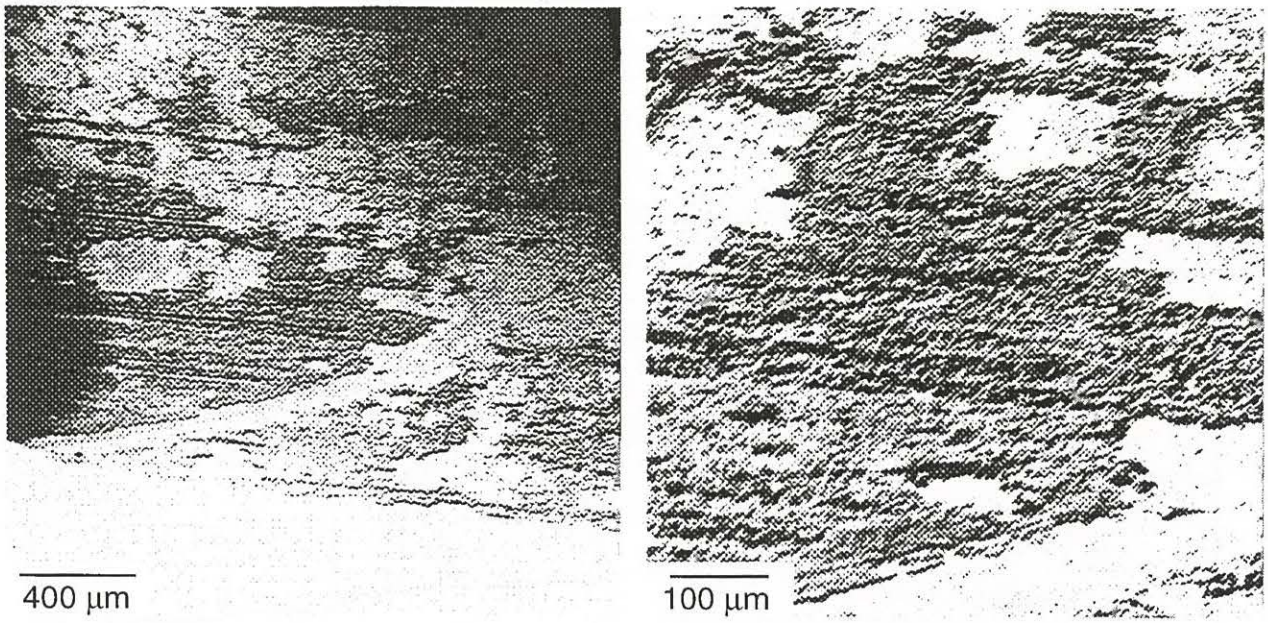

Figure 1. SEM Images Collected (at Increasing Magnification) from a Typical Area on the Inside Surface of the Fuel Sheath Toward the Bottom End of the Element. The Images Show Patches of Retained CANLUB (dark grey) as well as exposed sheath (light grey).

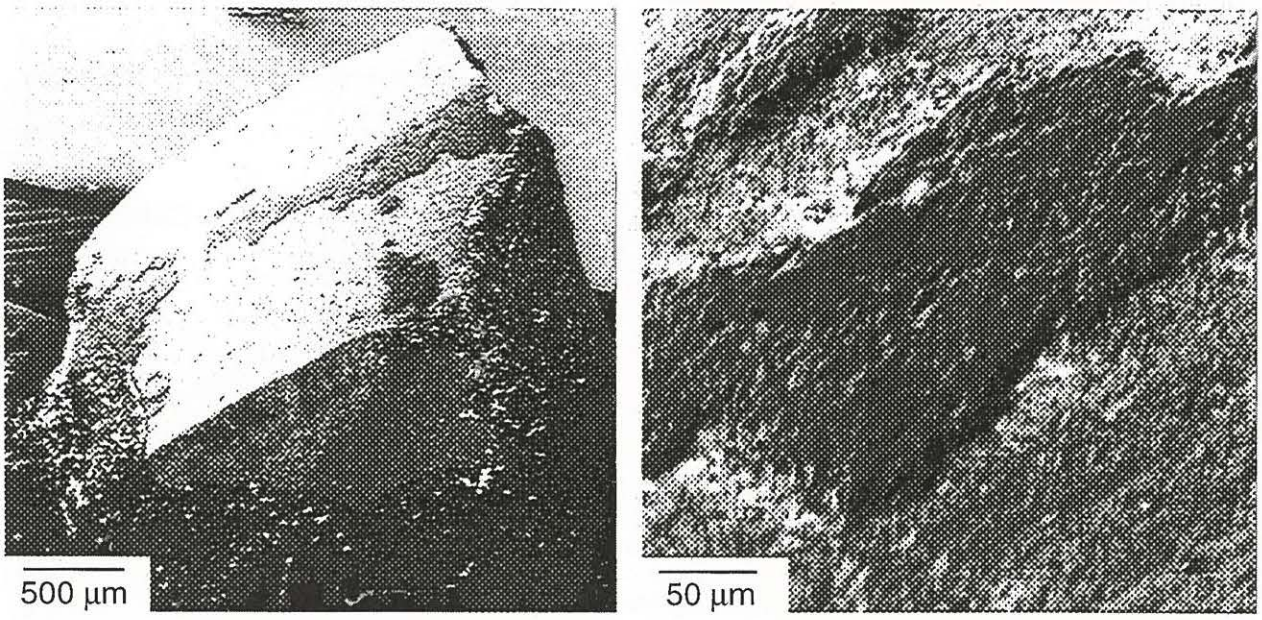

Figure 2. SEM Images Showing (at Increasing Magnification) Patches of CANLUB on the Surface of a Fuel Fragment Removed from Near the Middle of the Element. Conductive Silver-Based Epoxy Covers Part of the Fracture Face in the Foreground of the Image on the Left.

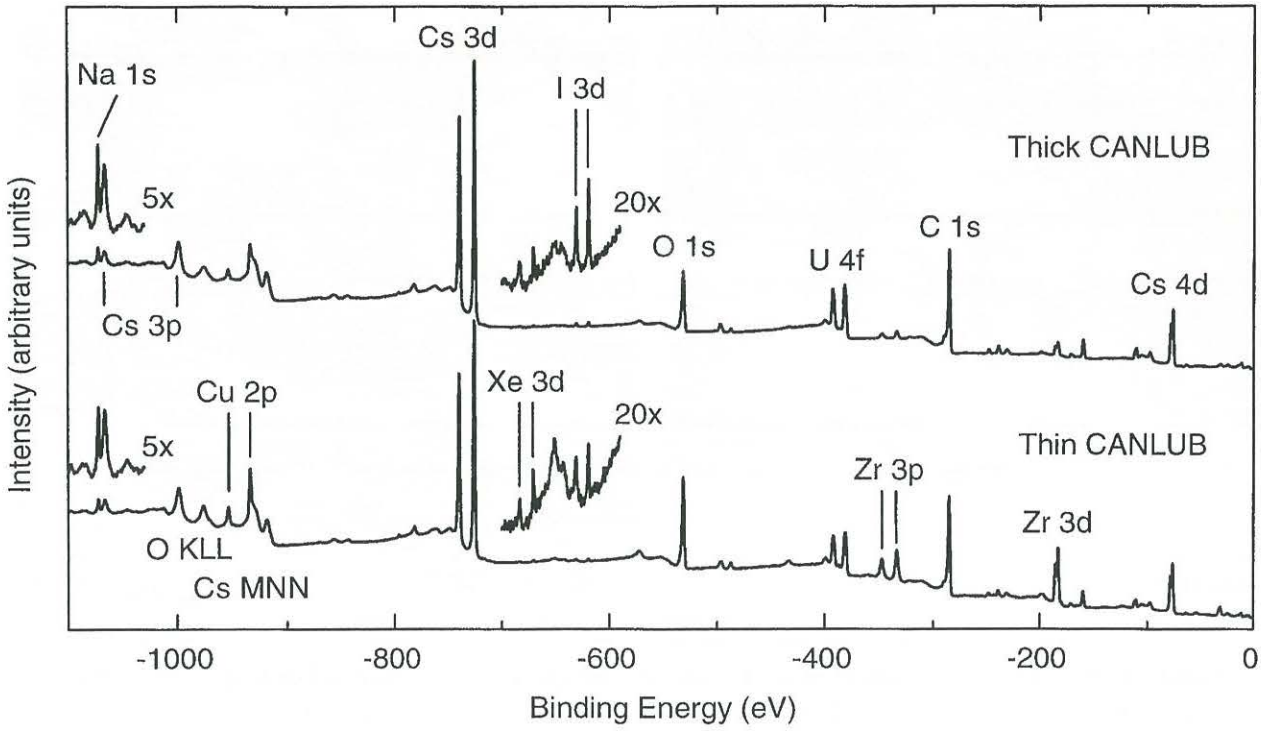

Figure 3. XPS Survey Spectra Recorded from Typical Regions (with Thick or Thin CANLUB Layers) on the Inside Surface of the Fuel Sheath, Toward the Bottom End of the Element.

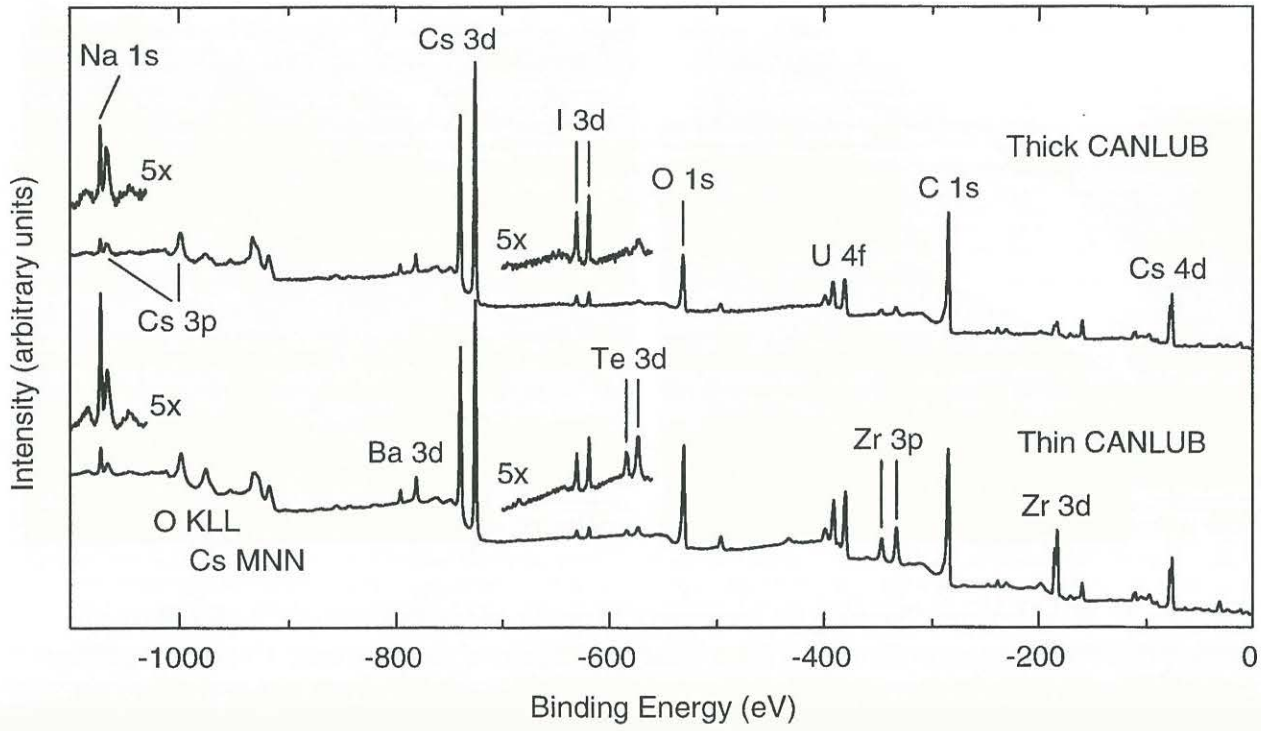

Figure 4. XPS Survey Spectra Recorded from Typical Regions (with Thick or Thin CANLUB Layers) on the Inside Surface of the Fuel Sheath, Toward the Top End of the Element.

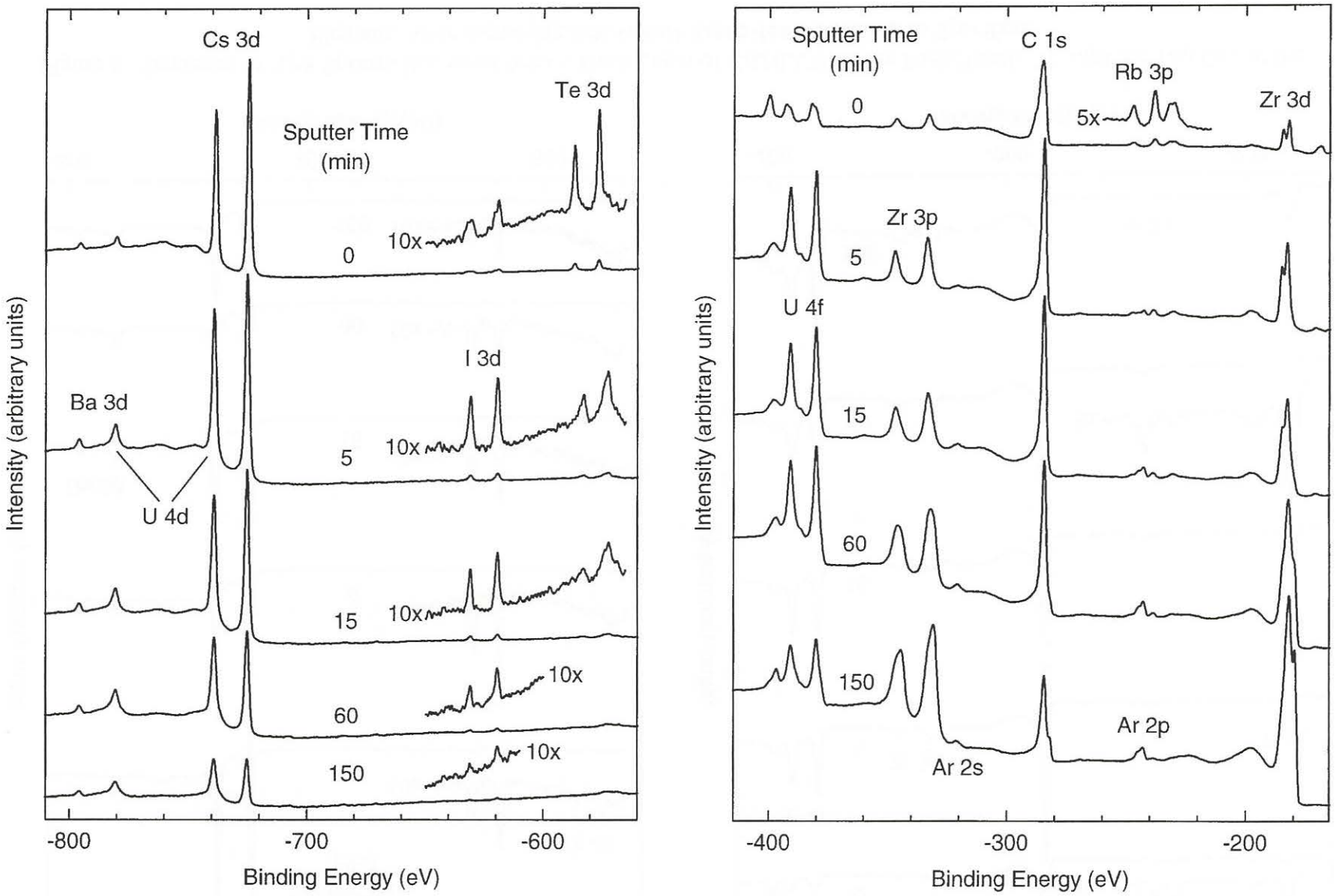

Figure 5. Sequence of XPS Spectra Recorded from a Region on the Fuel Sheath Without a Visible CANLUB Layer, Toward the Top End of the Element, After Increasing Intervals of Argon-Ion Sputtering as Specified.

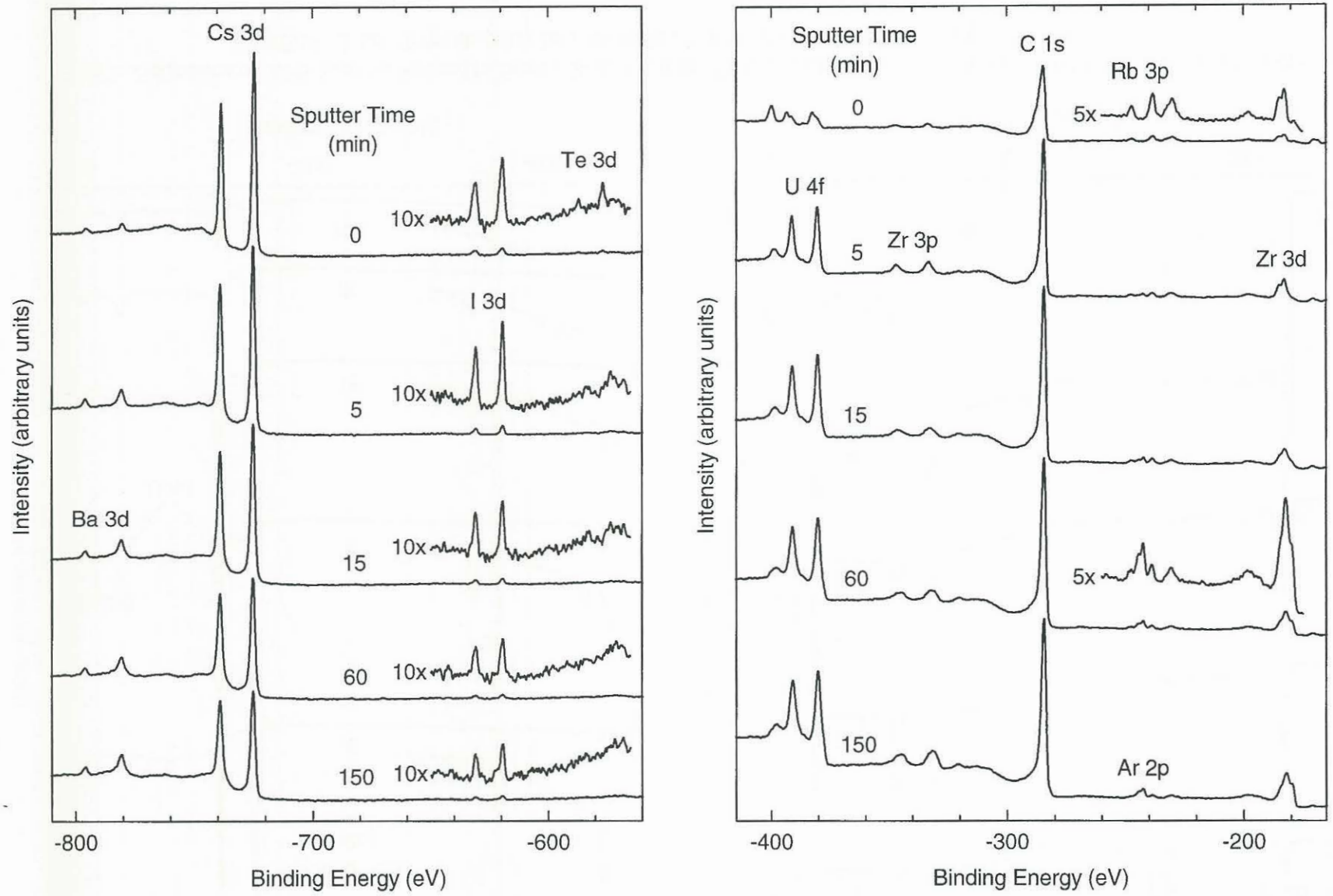

Figure 6. Sequence of XPS Spectra Recorded from a Thick Layer of CANLUB on the Fuel Sheath, Toward the Top End of the Element, After Increasing Intervals of Argon-Ion Sputtering as Specified.

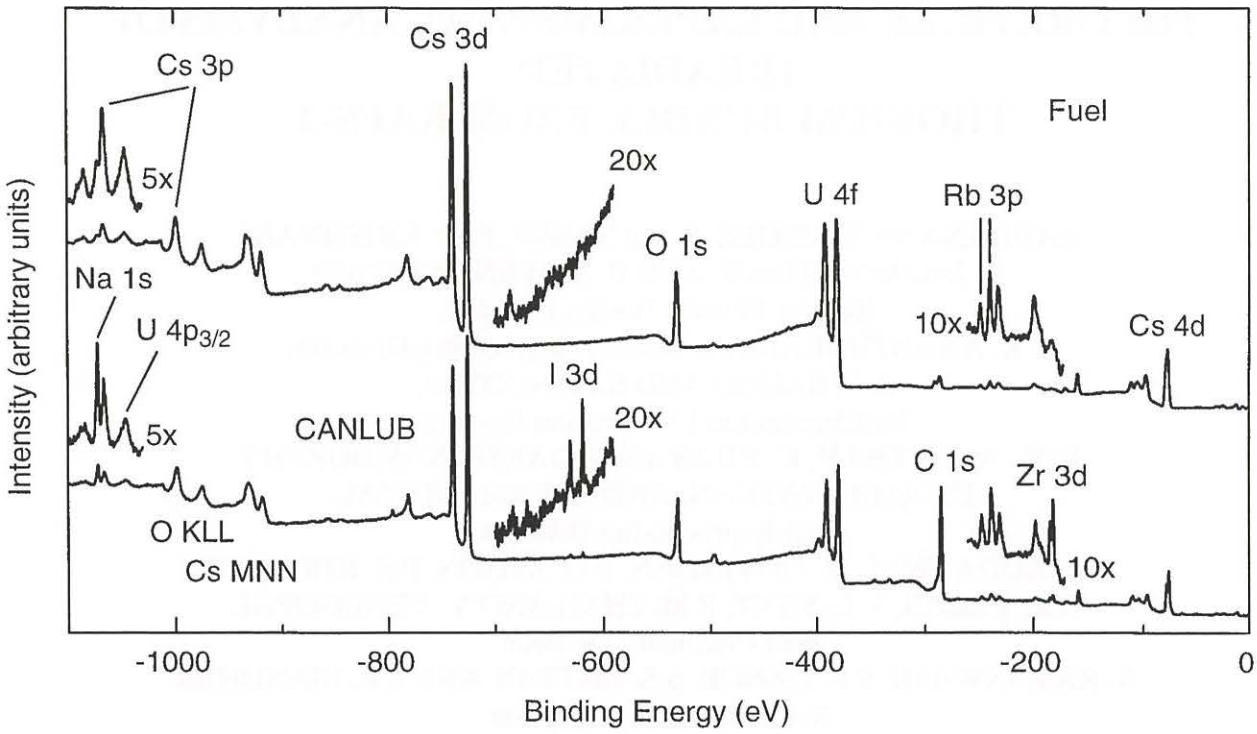

Figure 7. XPS Survey Spectra Recorded from Typical Regions (Exposed Fuel and a Patch of CANLUB) on the Periphery of the Fuel Fragment Shown in Figure 2.

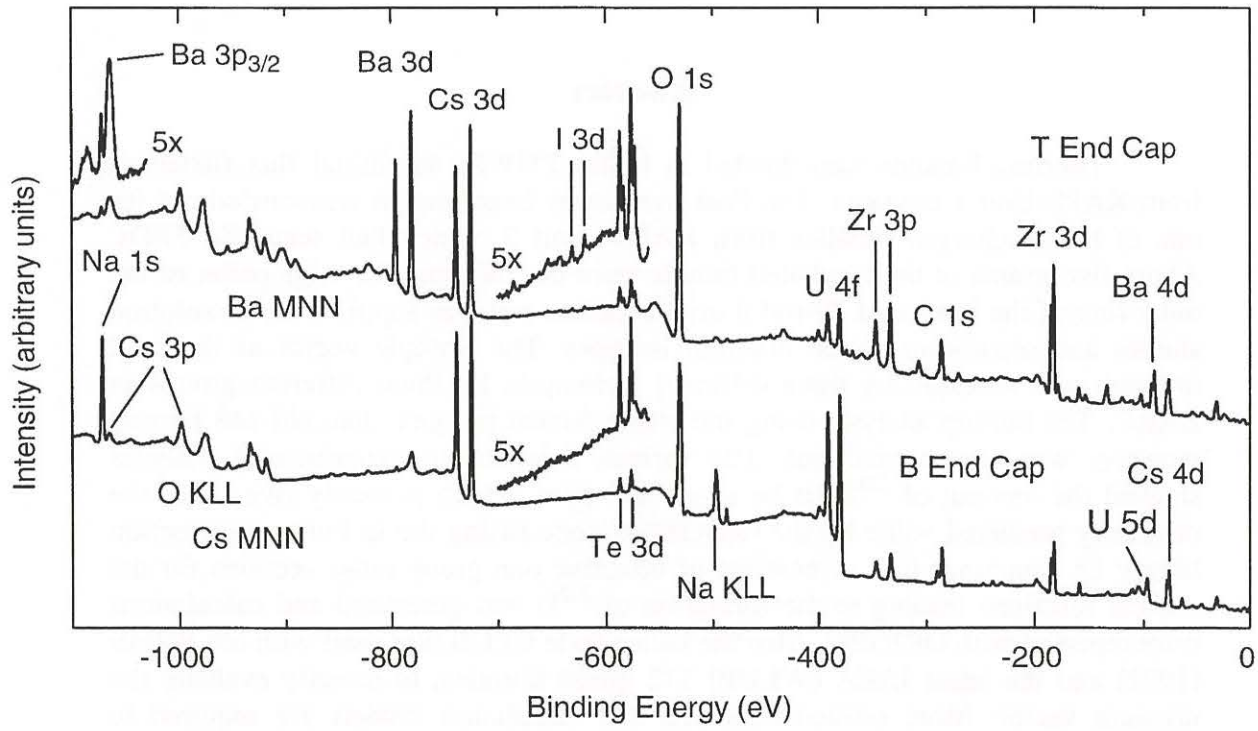

Figure 8. XPS Survey Spectra Recorded from Typical Regions on the Inside Surfaces of the End Caps Taken from the Top (T) and Bottom (B) Ends of the Element.